Dust detection mode of the Hayabusa2 LIDAR

Senshu, H. · S. Oshigami · M.
Kobayashi · R. Yamada · N. Namiki ·
H. Noda · Y. Ishihara · T. Mizuno

Abstract We aim to use light detection and ranging (LIDAR) to detect dust grains that might be present around asteroid (162173) Ryugu (1999 JU$_3$), the target of the Hayabusa2 mission. LIDAR is currently used for observing atmospheric aerosols on Earth by measuring the time profile of the return pulse (received light). In the case of Hayabusa2, LIDAR will be used only to determine whether the energy flux of the return pulse exceeds a certain threshold every 133.33 ns. This simplification significantly reduces the amount of down link data. The profile of the return pulse is estimated from iterative observations by changing the thresholds. Here, the performance of the dust counter mode is examined using a breadboard model, a flight model, and an engineering model. For these tests, we develop a new testing device to simulate various time profiles of the return pulse. We also estimate the lower bound of the number density of dust grains that can be detected. It is shown that the LIDAR on board Hayabusa2 is capable of detecting asteroidal dust if dust grains with size similar to the Hayabusa sample exist around the target body and their number density exceeds 10^5 m^{-3}.

Keywords Hayabusa2 · LIDAR · dust · asteroid · Ryugu

1 Introduction

The surface of the Moon is widely covered by dust grains, called regolith (McKay et al. (1991)). This is because the Moon does not have an atmosphere or water on its surface. As a result, its surface is exposed to micro- to planetary-sized impactors. The debris generated by impacts persists for a long

H. Senshu
2-17-1, Tsudanuma, Narashino, Chiba, JAPAN
Tel.: +81-47-478-4737
Fax: +81-47-478-0372
E-mail: hsenshu@gmail.com

time as small grains because cementation is inefficient without water under low-pressure conditions. Moreover, the rim of blocks on the lunar surface can fracture as a result of thermal stress caused by the daytime-nighttime temperature differences, which exceed 250 K (Delbo et al. (2014)). These effects are seen on asteroids, too, which also do not have an atmosphere or water on their surface. The Galileo spacecraft captured the first image of regolith on an asteroid during a flyby of (951) Gaspra. It has been suggested that regolith is common on asteroid surfaces (Thomas et al. (1994);Chapman (1996)). NEAR Shoemaker revealed that the surface of asteroid (433) Eros is covered by dust grains (Veverka et al. (2000)); the smooth surface of asteroid (253) Mathilde also indicates the presence of a surface dust layer (Clark et al. (1999)). However, it is not clear whether an asteroid with < 1 km size has dust grains on its surface. The image of asteroid (25143) Itokawa taken by Hayabusa reveals that the surface of this 330-m-size asteroid is covered by boulders. The smooth terrain on (25143) Itokawa, called Muses Sea, is composed of centimeter-sized pebbles (Miyamoto et al. (2007)). In the return samples, however, only dust grains smaller than 200 μm were found in the sample chamber of the re-entry capsule. Although the mechanism by which dust grains entered the sample chamber remains controversial, dust grains certainly exist on and perhaps around the surface of (25143) Itokawa.

An analysis of the exposure time of the Hayabusa dust sample to solar wind and cosmic rays demonstrates that (25143) Itokawa is losing its surface material over time, at the rate of tens of centimeters per million years (Nagao et al. (2011)). If asteroids commonly lose surface material into space, they will contribute to the zodiacal dust cloud . Even when a dust grain fails to escape the gravitational field of its parent asteroid, the mass movement can create specific landforms such as the 'pond' on (433) Eros (Veverka et al. (2001)). In addition, dust grains floating above the surface may be hazardous to spacecraft during touch down and sampling maneuvers. Owing to these operational conditions and the scientific goals to be achieved, we added a new operational mode to the light detection and ranging (LIDAR) module on board Hayabusa2 (hereinafter, simply called 'LIDAR') to enable it to detect dust grains by remote sensing.

Hayabusa2 is Japan's second mission to an asteroid. It was successfully launched from Tanegashima Space Center (TNSC) on 3 December 2014 at 13:22:04 (UTC+9) by H-IIA rocket. The target of the Hayabusa2 mission is the near-Earth asteroid 162173 Ryugu (1999 JU$_3$). Its semi-major axis is 1.189 AU and eccentricity is 0.19; therefore, its perihelion (0.963 AU) is inside the orbit of Earth and its aphelion (1.415 AU) is near the orbit of Mars. Its albedo is estimated to be as low as 0.05, and the reflectance spectrum obtained by ground-based observation is featureless and flat at visible and near-infrared wavelengths. As a result, it is classified as a C-type asteroid. After rendezvousing with the asteroid in mid 2018, Hayabusa2 will maintain a distance of $\sim$ 20 km, except when performing special operations such as high-resolution mapping; rover, lander, impactor release; and touch down to

the surface for sampling surface material. Hayabusa2 will leave the asteroid in late 2019 and return to Earth in late 2020.

LIDAR is one of the modules on Hayabusa2. It can be used to measure the distance from the asteroid in the range from 25 km to 30 m (Namiki et al. (2012); Mizuno et al. (2015); Yamada et al. (2015)). The former is the upper bound on the 'home position' where Hayabusa2 will stay in the nominal phase (Okada (2012); Tsuda et al. (2013)), and the latter is the distance Hayabusa2 will approach for touch down and sampling. Within a distance of 50 m, a laser range finder (LRF) is used to measure the altitude instead of LIDAR (Tsuda et al. (2013)). Thus, LIDAR needs to cover a dynamic range wider than six orders of magnitude of return pulse energy.

LIDAR has two optics, one for long range (≥ 1 km) and the other for short range (< 1 km). The dynamic range of the analog-to-digital converter (ADC) behind each of the receiver optics (avalanche photo diode [APD]) and amplifier is limited to 8 bits. We selected three levels of high voltages to the APD such that the LIDAR covers the entire distance range from 25 km to 30 m. We use the wide dynamic range of the LIDAR and add a new functional mode to it to detect dust grains that might be present around the asteroid by detecting the faint scattered light from dust grains along the line of sight. For more details about the basic performance of the LIDAR, see Mizuno et al. (2015).

2 Dust detection mode of LIDAR on board Hayabusa2

In terrestrial atmospheric observations, LIDAR is used to measure the distribution of aerosol grains along the line of sight. The profile of the return pulse is analyzed using the LIDAR equation (given in Sec. 5). However, in the case of Hayabusa2, the energy profile is too large to be down-linked to Earth, because the link budget between the spacecraft and the ground station is quite limited. To reduce the data size, we applied the following measures: (1) the dust count range is limited to a part of the line of sight, (2) this dust count range ($d2$ in Fig. 1) is divided into 50 bins, and (3) the power of the signal (solid curve in the lower panel of Fig. 1) in each bin is compared with a certain threshold (horizontal dashed line in the lower panel of Fig. 1). The size of the observation data is only 50 bits for each shot. The length, or duration, of each bin needs to be larger than the response time of the APD or the circuit behind it. Additionally, if the length of each bin is kept too short, the total range of observations becomes too narrow. On the basis of the scientific requirement that the temporal resolution of the dust count be as high as possible, we set the duration of each bin to a constant value of 133.33 ns, corresponding to a spatial resolution of 20 m, resulting in a total observation range of 1 km (see Fig. 1). The distance to the initial point of the dust count range ($d1$ in Fig. 1) can be varying the wait time, which can be set by one command between 0 and 127 μs in increments of 1 μs. This corresponds to changing of $d1$ from the vicinity of the spacecraft to a distance of 19.05 km from the spacecraft in units of 0.15 km. We can therefore search for signs of dust around the target
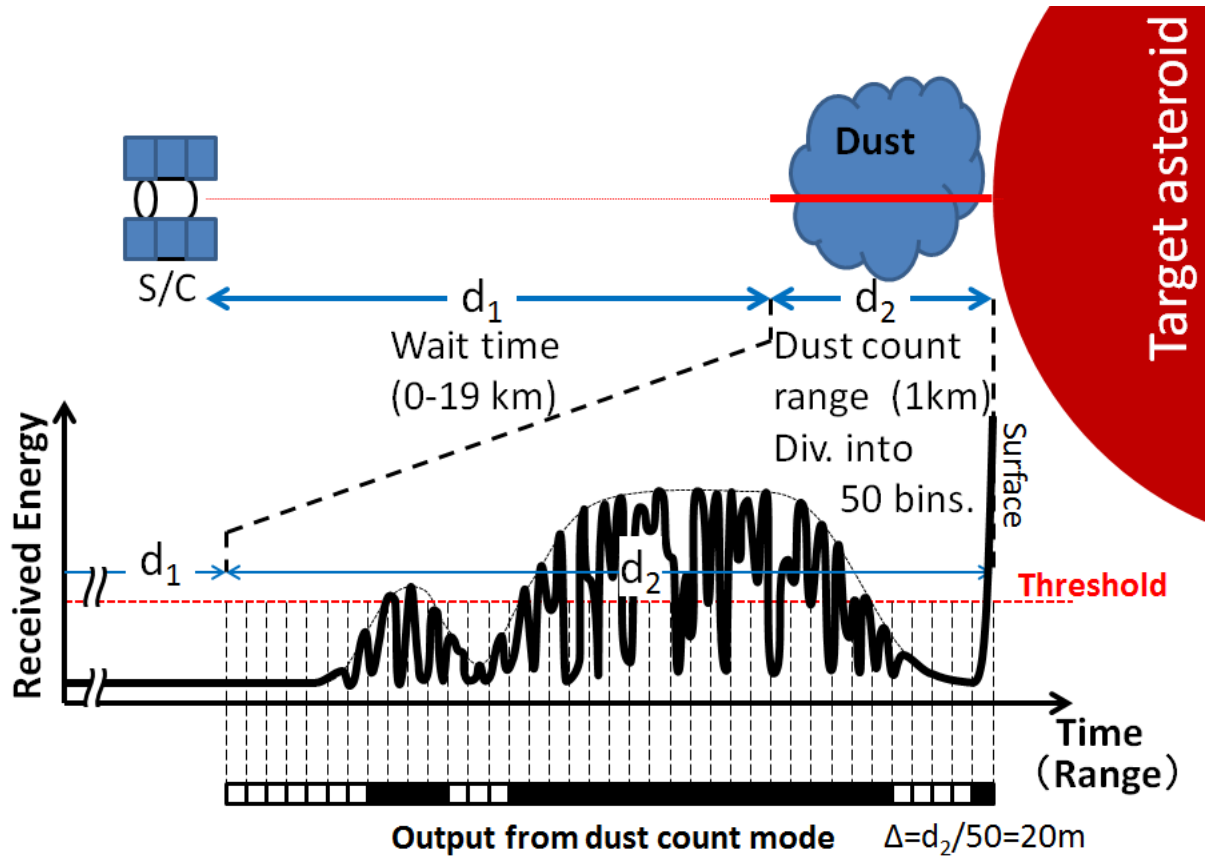
Fig. 1 Schematic view of dust count mode. In this figure, d_1 represents the distance from the spacecraft to the initial point of the observation range, and d_2 represents the observation range (width: 1 km). The time profile of the return pulse from the dust grains is expected to be noisy, like the solid curve shown in the lower panel. In this case, we obtain a black/white (1/0) output as shown at the bottom of the figure.

asteroid even from an altitude of 20 km (see Fig. 1). However, it should be noted that the farther the dust count range is set, the fainter the signal from the dust grains becomes because of geometric attenuation. Therefore, we will try to detect dust grains from as low altitude as possible.

The 50-bit data observed by one shot (one LIDAR measurement) is given by the specified threshold and is insufficient for estimating the energy profile of the return pulse (see Fig. 1). We use multiple shots at different threshold voltages so that we can roughly estimate the energy profile of the return pulse (see Fig. 2).

The threshold voltage is compared with the output voltage behind the receiver optics (APD) and amplifier (Mizuno et al. (2015)). The LIDAR provides 64 sets of threshold voltage for far range optics, two of which are used for nor-
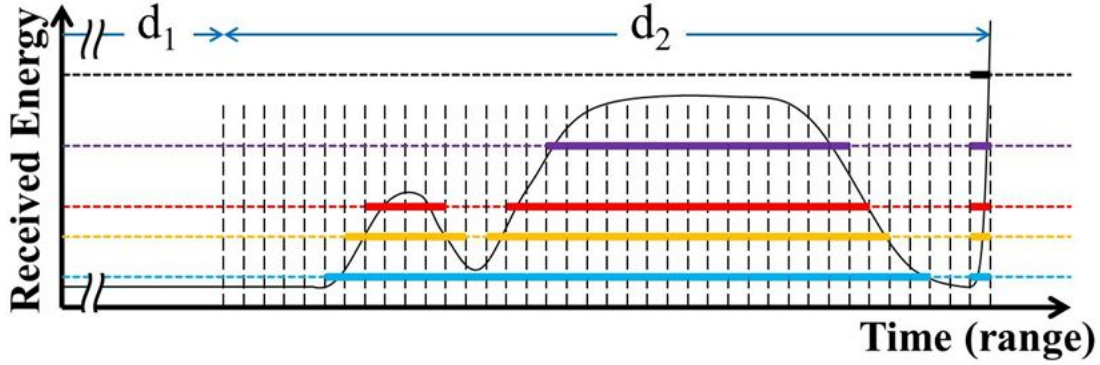
Fig. 2 Schematic view of dust count mode with varying threshold voltage. Vertical broken lines represent the boundaries of observation bins. Horizontal dashed lines represent threshold voltages, and solid lines on the dashed lines represent bins where a dust signal is detected. The thin curve represents the estimated time profile from these results, which is similar to the envelope of the original noisy pulses indicated by the thin dotted curve in Fig. 1.

Table 1 Threshold voltages of 'key' thresholds.

threshold #, n	0	1	2	4	8	16	32	40	63
$V_{\text{th},n}$, mV	3923.8	11.4	16.8	30.9	37.3	86.2	96.6	27.1	4.4

mal ranging. Each threshold voltage is set by six open/closed switches (inset of Fig. 3). The resulting threshold voltage, $V_{\text{th},n}$, is calculated as follows:

$$\frac{1}{V_{\text{th},n}} = \frac{1}{V_{\text{b}}} + \sum \frac{\delta_i}{V_i}, \tag{1}$$

where V_{b} represents the threshold voltage of mode 0 (baseline); V_i, the corresponding threshold voltage of the i-th switch; and δ_i, whether the i-th switch is closed (1) or open (0). The threshold number, n, is given by $\sum \delta_i 2^{i-1}$. Table 1 lists the key threshold voltages that are particularly important for estimating the number density of asteroidal dust. Fig. 3 shows a series of threshold voltages sorted by value. The minimum value of the threshold voltage is 4.4 mV (threshold number 63), which is around one-seventh the threshold voltage used in the normal ranging mode, 27.1 mV (threshold number 40).

3 Development of testing device

To evaluate and calibrate the dust detection mode described in the previous section, we performed ground tests using the test configuration shown in Fig. 4. In this testing, we need to simulate the backscatter of the transmitting laser by floating dust particles as an input to the receiver telescope of the LIDAR.
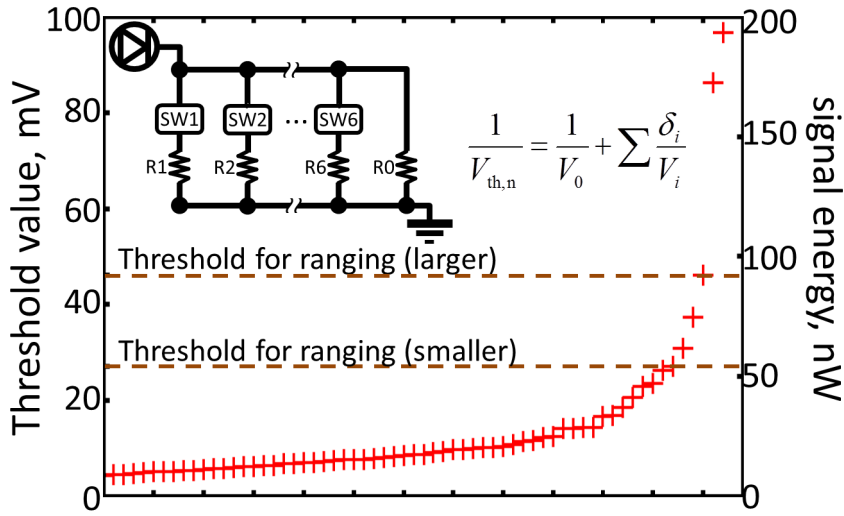
Fig. 3 A series of threshold voltages sorted by value. The larger and smaller threshold voltages are 27.1 mV (threshold number 40) and 46.1 mV (threshold number 48), respectively.

For this purpose, we developed a portable testing device that emits arbitrarily patterned laser light pulses. Fig. 5 shows the testing device, registered as ALT-9C74 (serial number 3101, ALT Co., Ltd., In Tokyo, Japan) for commercial use.

The ALT-9C74 is a laser pulse generator for 3-bit digital patterns with a programmable laser power level. It operates at a clock rate of 100 MHz for a sequence of 256 numerals after it is triggered externally. Specifically, individual laser pulses are emitted every 10 ns for 2.56 μs and have variable levels from 0 to 7. The ALT-9C74 consists of a laser diode (LD), three constant-current power supplies for driving the LD at three levels of power, and an FPGA for controlling the three current sources. Normally, an automatic power controller (APC) is used for driving the LD; however, the APC cannot respond quickly enough to simulate the backscatter of laser light.

The ALT-9C74 has a maximum laser power of around 10 mW. In the test configuration shown in Fig. 4, multiple neutral density (ND) filters are placed between the ALT-9C74 and the LIDAR to fit the laser power to the acceptable range of the LIDAR receiver. The ND filters can be attached at the aperture of light emission using a C-mount thread (see Fig. 5). The beam divergence angle of the emitted light is arranged to be less than 1 mrad so that it is within the 1.5 mrad field of view of the LIDAR (Namiki et al. (2012); Mizuno et al. (2015); Yamada et al. (2015)).

In the test configuration shown in Fig. 4, the ALT-9C74 emits a laser light pulse at the timing of a logic pulse input from the pulse generator, so that
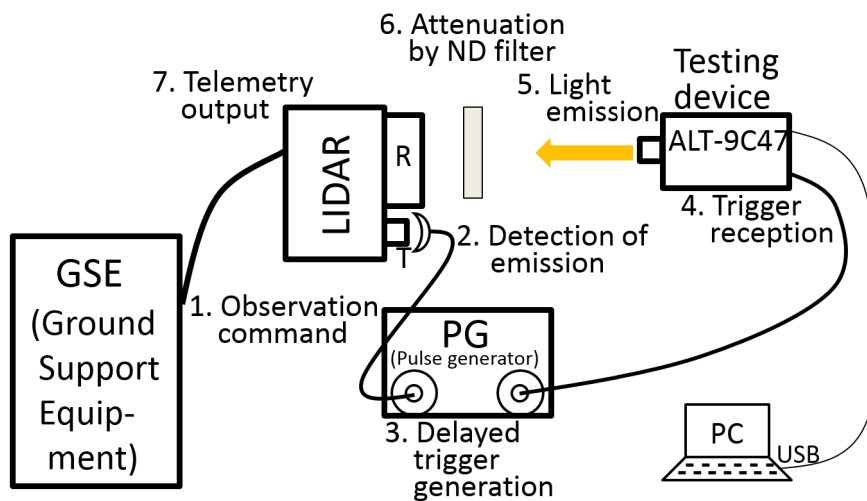
Fig. 4 Schematic of function test settings by using the testing device. In this figure, 'T' and 'R' represent the laser transmitter and optical receiver of the LIDAR, respectively. The numbers indicate the flow of optical and electrical signals.
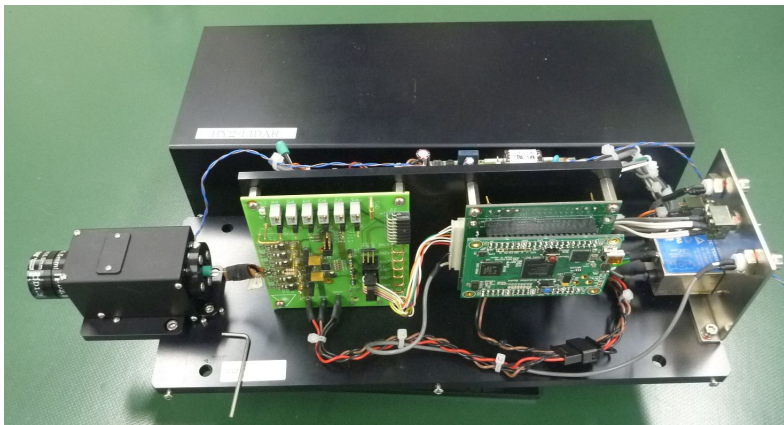
Fig. 5 Photo of the ALT-9C74 testing device. In this figure, the device is uncovered and the cover is placed behind the device. Once a trigger signal input (4 in Fig. 4) is received via a connector on the right-hand side, the ALT-9C74 emits output light (5 in Fig. 4) to the left-hand side. In this photo, two C-mount thread filters are attached at the end of optical system.

the transmitted pulse is emitted with a delay corresponding to the distance between the LIDAR and the laser scatterers.

4 Function test of the LIDAR

During the development of the flight model (FM), the LIDAR was tested repeatedly to check its function. Science team members also attended these tests to examine its performance and noise levels.

4.1 Electric test

Before the integration of the LIDAR, a breadboard test was carried out by NEC Corp. In this test, a rectangle electric pulse with time duration of 10 ns was input to the circuit behind the receiver optics to confirm that the circuit identified the signal in an appropriate bin. The timing of the electric input was shifted in sequence from the first bin to the last bin for a given wait time. The same test was repeated for different wait times from 0 to 127 μs to prove that every input was detected in the correct bin. We confirmed that the circuit detects the input signal in the correct bin as long as the input signal is a single pulse.

4.2 Function test using the ALT-9C74

After integrating the LIDAR, function tests were performed using the ALT-9C74 to confirm the three functions of the LIDAR's dust count mode, namely, stability and reproducibility of the detection timing of the signal, sensitivity to various thresholds, and detection of long pulses. These tests performed after the launch of Hayabusa2 using the engineering model (EM) of the LIDAR. The optical receivers and the circuit behind the receivers of the EM are constructed from the same elements as the FM. The software installed in the FPGA of the EM is also identical to that installed in the FM. Thus the performance of the dust count mode of the EM is equivalent to that of the FM. However, it should be noted that these tests were performed in a laboratory. In general, laboratory tests are affected by noise to a great extent than in-flight tests owing to unstable thermal and electrical conditions.

The stability and reproducibility of the detection timing for multiple pulses were tested using the ALT-9C74. The shape of the pulses is shown in Fig. 6. In this test, each pulse had seven (maximum) power levels because the main purpose of this test was to confirm the detection timing. The arrival of a signal was controlled by the time difference between the delay time within the pulse generator (3 in Fig. 4) and $d1$ in Fig. 1. We varied the delay time of the pulse generator (0.6, 2.8, and 5.0 μs) while keeping the wait time constant at 1 μs so that the observation range was covered by three sets of light emissions.

Fig. 7 shows the resulting output for an input of repetitive pulses. Stable signal timing was obtained during this test. For a delay time of 0.6 μs (left panel of Fig. 7), an initial signal was beyond the dust count range because the wait time of the dust count mode in this test is 1 μs. The result for a delay

Fig. 6 Schematic image of the relation between timing of repetitive pulses and sampling rate of the dust count mode.

Fig. 7 Resulting output for input of repetitive pulses as shown in Fig. 6. A row represents 50 sets of 0/1 outputs ('1' is hatched for emphasis), and a column represents the time-series of observations. The delay times are 0.6 μs (left), 2.8 μs (center), and 5.0 μs (right).

Fig. 8 Averaged value of output for input of repetitive pulses, as shown in Fig. 7. The averaged value is multiplied by 9 so that the values are given as single-digit numerals. Each bin is hatched depending on the value. The delay times, τ, are 0.6 μs (upper), 2.8 μs (middle), and 5.0 μs (lower).

time of 2.8 μs demonstrates a shift of $16-17$ bins relative to the results for 0.6 μs. This shift is expected given that each bin has a distance in time of 133.33 ns (133.33 ns $\times$ 16 = 2.13 μs). In this test, the signal emitted from the ALT-9C74 contained 9 pulses in 2560 ns (Fig. 6). If both the pulse width and fall time of the circuit are negligible, the resulting output should be composed of nine 1's. However, because of both the finite pulse width and finite fall time of the circuit, a pulse can be detected in up to two bins. In addition, there is jitter of less than 1 bin. As a result, the output data contains 10 to 12 of 1's for each shot. The averaged value of the output data is shown in Fig. 8. The value of each bin is multiplied by 9 so that the detection frequency is represented by one-digit numerals, 0 to 9. Fig. 8 shows nine peaks along the line of sight; however, some of them are broadened by $1-2$ bins. Thus, it was confirmed that the LIDAR detects signals with a resolution of 2 bins.
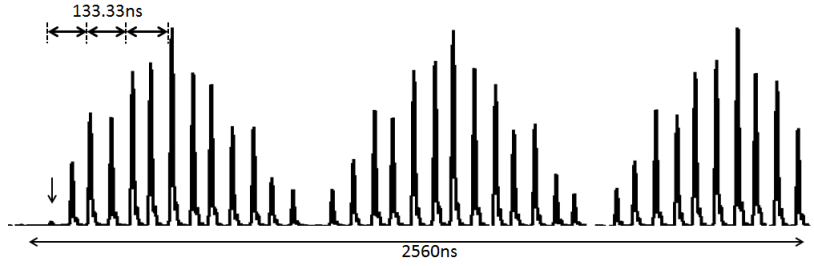
Fig. 9 Time profile of three-peaks signal as measured by a PIN photo diode with fast response and a bandwidth of 1 GHz. The width of each pulse is 10 ns.
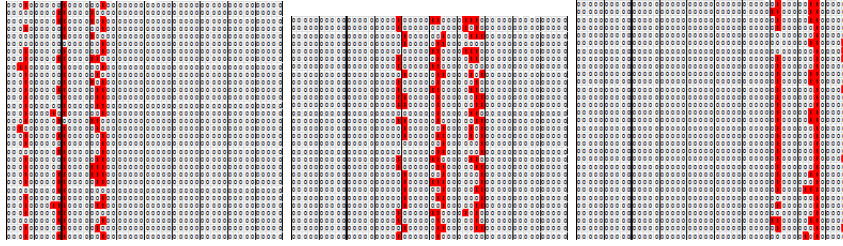

Fig. 10 Resulting output for the input of three mounds composed of multiple pulses (Fig. 9) with delay time of 0.6 μs (left), 2.8 μs (center), and 5.0 μs (right). In this test, the threshold voltage is 27.1 mV (threshold number 40).

Next, we tested the dependency of the output on various thresholds. The profile of the simulated return pulse is shown in Fig. 9. The light emitted from the ALT-9C74 in this test comprises multiple pulses, and its envelope is composed of three peaks. For technical reasons, the peak energy of each pulse is not equally distributed, and the first pulse shrinks (indicated by an arrow). We performed dust count mode observations with the three delay times mentioned above as well as four thresholds: 4.4, 14.5, 27.1, and 37.3 mV. The results are shown in Figs. 10-13. Three groups of signals were obtained for all cases, and signals were more clearly visible with a lower threshold. However, for the case with a threshold of 4.4 mV (threshold number 63), a static wave form 'tail' appeared after the peaks. Because spurious signals did not appear before the envelope peaks, they were not thermal noise. At the same time, the initial rise of the received pulse could be detected with a threshold voltage as low as 4.4 mV because the level of thermal noise appeared to be lower than 4.4 mV. Fig. 14 shows an averaged 1/0 pattern multiplied by 9 for the input of three envelope peaks for three wait times and four threshold voltages.

The resulting signal is compared with the input signal in Fig. 15. The left panel of Fig. 15 shows the extracted data from the 16th to the 30th bins of the averaged value for a wait time of 2.8 μs (Fig. 14) on a time-threshold plane. The input signal from the ALT-9C74 (Fig. 9) is overlaid on the graph of the
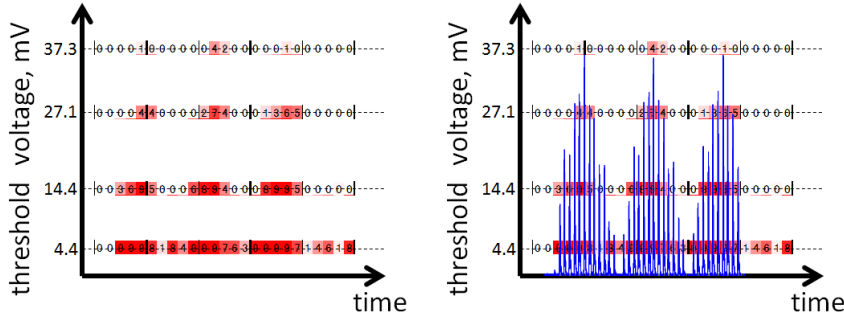
Fig. 11 Similar to Fig. 10 but for a threshold voltage of 37.3 mV (threshold number 8).

Fig. 12 Similar to Fig. 10 but for a threshold voltage of 14.5 mV (threshold number 44).

Fig. 13 Similar to Fig. 10 but for a threshold voltage of 4.4 mV (threshold number 63).

Fig. 14 Averaged output value for the input of three peaks as shown in Figs. 10-13. The averaged value is multiplied by 9 so that the values are given as single-digit numerals. Each bin is hatched depending on the value. The delay times, τ, are 0.6 μs (upper), 2.8 μs (middle), and 5.0 μs (lower).

Fig. 15 (Left panel): 'Average' of the output of the dust count mode as a function of the threshold voltage. The averaged value are multiplied by 9 so that the values are obtained as single-digit numerals. Each numeral is hatched depending on the value. (Right panel): The time profile of the input light is overlaid for comparison. It should be noted that the vertical range of the time profile of the input light is scaled to match the pattern of the output signal.

averaged pattern in the right panel of Fig. 15. Through a comparison of the resulting signal with the input signal, a rough profile of the three peaks was obtained from this series of observations. However, a ghost 'tail' appeared for cases with a threshold voltage of 4.4 mV. The reason why the 22th bin (7th bin in Fig. 15) remains 0 although the ALT-9C74 emits light at this timing remains unclear. A similar tendency was also seen in tests with another wait time (Fig. 14). More tests are needed to clarify this issue.

Finally, the detectability of a long pulse was tested. In this test, the simulated return pulse had a rectangular profile with a duration of 1 μs. The results are shown in Fig. 16. The LIDAR detected the rise and fall of the signal, but failed to detect the signal in between. This is because the analog circuit behind the receiver optics works as a high-pass filter. The LIDAR circuit cannot detect a flat signal, and thus, it is insensitive to long pulses. Additionally, the fall signal was located at the 6th bin from the initial rise in some cases and at the 10th in other cases. The LIDAR correctly detected the fall signal around 1 μs after the initial rise. However, in the latter case, the fall signal was detected 1.3333 μs after the initial rise. The reason for the two 'tail' patterns remains unclear. Further experiments are needed to understand the mechanism of 'tail' occurrence and to predict the conditions.

5 Numerical simulation of the return pulse energy from dust scattering

Because we cannot determine the amount of dust around the target body in advance, dust detection is performed with a best-effort operation. Here, we calculate the energy of the returning pulse reflected from dust using the Mie
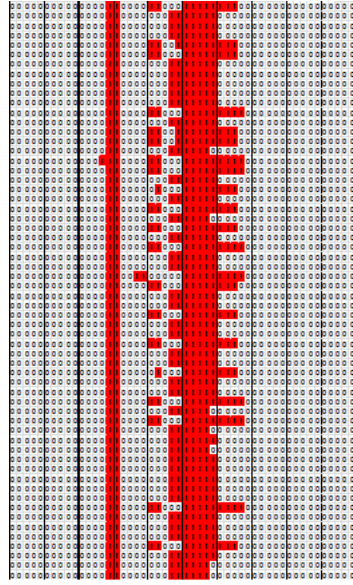
Fig. 16 Resulting output for a long pulse with duration of 1 μs. In this test, the delay time is set to 2.2 μs so that the entire simulated return pulse is involved in the dust count range.

scattering model. Here, we assume that the diameter of the dust is larger than the wavelength of the laser, that is, 1064 nm. The characteristic distance between dust grains is assumed to be sufficiently larger than the wavelength so that interaction between dust particles is negligible. We also assumed that dust clouds float close to the surface (at a height of tens of meters). By using the LIDAR equation (eq. (2)), we estimated the return peak power, P_r, of backscattered light from a dust cloud for various sets of distance, h, dust number density, N, and dust size distribution, $N(a)$. (e.g., Bohren and Huffman (1983); Liou (2002)). Tables 2 and 3 show a description of each parameter in eqs. (2)-(5).

$$P_r = P_0 e T_t T_r \frac{c\Delta t}{2} \frac{\pi D_r^2}{4h^2} \frac{\beta}{4\pi}, \tag{2}$$

$$V_r = P_r \times R_{pd}, \tag{3}$$

$$\beta = \int_{a_1}^{a_2} S_b(a) \frac{dN(a)}{da} da, \tag{4}$$

$$S_b = \frac{\pi}{\kappa^2} \left| \sum_{n=1}^{\infty} (-1)^n (2n+1)(A_n - B_n) \right|^2, \tag{5}$$

where A_n and B_n are Mie scattering coefficients that are known to depend on the complex dielectric constant of the scatter (see Bohren and Huffman (1983) and Liou (2002) for derivation). We assume that the complex dielectric

Table 2 Parameter values relevant to dust count prediction.

Symbol	Parametere	Unit	Value
P_r	Return power	W	eq. (2)
V_r	Output voltage of detector	V	eq.(3)
c	Velocity of light in vacuum	m/s	3.0×10^8
Δt	Laser pulse width	s	5.6×10^{-9}
κ	Wave number of laser pulse	-	5.91×10^6
P_0	Laser output peak power	W	2.4×10^6
e	Laser energy availability	-	0.411 (nominal case)
h	Range	m	$10^3, 5 \times 10^3, 20 \times 10^3$
T_i	Optical efficiency of laser transmitter	-	0.894
T_r	Optical efficiency of receiver	-	0.678
D_r	Effective radius of telescope	m	0.11
R_{pd}	Detector responsivity	V/W	4.98×10^5

Table 3 Assumed values of physical properties for dust grains.

Symbol	Physical character	Unit	Value
a	Dust radius	m	$5 \times 10^{-7} - 5 \times 10^{-5}$
N	Dust number density	m^{-3}	$10^4 - 10^{10}$
β	Volume backscatter coefficient	m^{-1}	eq.(4)
S_b	Mie backscatter cross-section	m^2	eq.(5)

constant of dust particles is the same as the typical values for soot or dirty silicate cosmic dust analogs at visible wavelengths: $2.40 + 2.38i$ (Michel et al. (1996)). Fig. 17 shows the expected peak output voltages resulting from the received reflection from dust clouds with a homogeneous size distribution.

According to Fig. 17, the number density of dust grains with size similar to that of the Hayabusa sample ($\sim 40\ \mu$m) is required to be larger than 10^8 m^{-3} to be detectable from an altitude of 20 km ('home position'). When the spacecraft descends to an altitude of 1 km, the lower limit of the number density decreases to 10^5 m^{-3}. For dust grains with a size of 5 μm, the lower limits are 10^{10} m^{-3} and 10^7 m^{-3} for the 20 km and 1 km altitude cases , respectively.

6 Observation plan using dust count mode

The dust count mode of the LIDAR is used to explore the dusty environment around Ryugu. The maximum range of the dust count mode is up to 20 km. This means that we can observe dust clouds just above the surface of the target body from the home position. Whether ghost 'tail' appears in space can be confirmed by observations using the dust count mode from the home position, where the return pulse from the surface of the target asteroid is strong enough to be detected in the normal ranging mode. It should be noted that if the return pulse from the dust grains is as strong as that from the surface of the target asteroid, the presence of the dust cloud could be confirmed by on board cameras.
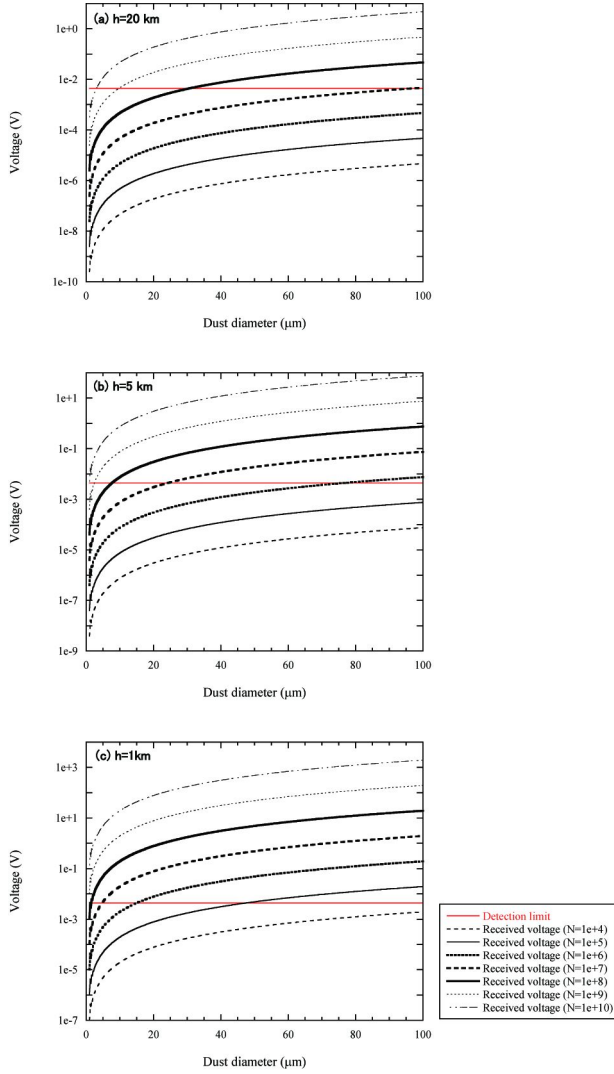
Fig. 17 Expected peak output voltage of detector versus dust diameter when the flight altitude is (a) 20 km (home position), (b) 5 km, and (c) 1 km, respectively. Each curve indicates a different dust number density (N in Table 3). The detection limit (4.4 mV) of the detector is also shown.

Several mechanisms have been proposed for dust floating above an asteroid surface (e.g., Richardson et al. (2004)): electrostatic force, solar-wind pick-up, oscillation of the asteroid owing to impacts or tides, and others. Hartzell and Scheeres (2011) argued that a dust grain smaller than 100 μm cannot detach from the surface because the smaller the dust grain, the more effective is the cohesive force relative to gravitational or electrostatic forces. On the

other hand, Kimura et al. (2014) noted that the restriction on dust floating due to electrostatic force can be relaxed by taking into account dust agglutinate and/or geometric effects, especially at the terminator (daytime-nighttime boundary). Recently, the Lunar Dust Experiment (LDEX) an impact ionization dust detector on board the Lunar Atmosphere and Dust Environment Explorer (LADEE) mission, performed a search for small ($\sim 0.1~\mu$m), high-altitude dust grains floating above the lunar sunrise terminator and found no evidence for the putative population (Horányi et al. (2015); Szalay and Horányi (2015)). It should be noted that this result does not rule out the existence of dust grains at low altitude (< 3 km). Therefore, we plan to search for floating dust above the terminator region.

As shown in the previous section, the received energy of scattered light from dust grains becomes stronger when the dust grains are closer to the LIDAR. We should therefore make the most of the opportunities available when Hayabusa2 descends to the target body, such as during the touch down maneuver and its rehearsal. The purpose of the rehearsal is to confirm the procedures required for the touch down maneuver as well as to verify the safety of the target area for the spacecraft. Thus, floating dust grains around the target area should be searched for in advance to avoid a possible hazard to the spacecraft.

In addition to the touch down and its rehearsals, Hayabusa2 will descend to release a rover, landers, and a small carry-on impactor (SCI). Furthermore, the landing of the rover and landers could produce floating dust in the vicinity of landing points. Observation of such floating dust would provide useful information for estimating the cohesive force between dust grains and the surface.

At the time of the SCI explosion Hayabusa2 will be positioned on the opposite side of the asteroid to avoid being hit by any debris. Thus Hayabusa2 cannot observe the impact or ejecta directly. However, after the impact, a fraction of the ejecta will be accelerated by solar wind and may pass by Hayabusa2. Thus, we plan to operate the LIDAR in the dust count mode although Hayabusa2 cannot face the asteroid owing to power generation restrictions. If the number density of the ejecta is sufficient, the LIDAR will detect a signal from the dust grains. The efficiency of the acceleration by solar wind is highly dependent on the size of the dust grains. Thus the time profile of the dust number density may provide information on the size distribution of the ejecta.

7 Conclusions

In addition to measuring the distance between the spacecraft and the target body, the LIDAR on board Hayabusa2 is capable of detecting dust clouds above the target body's surface.

Through the series of function tests described above, we confirmed that the LIDAR correctly detects the timing of the initial rise of a simulated return pulse. According to our simple estimation, we can detect dust grains with a

size similar to those contained in the Hayabusa sample. The detection of dust grains is expected to be enhanced when the spacecraft descends toward the surface. This is useful not only for scientific purpose but also for assessment of any hazards they may pose to the spacecraft.

However, some problems remain unsolved. The appearance of a ghost 'tail' after the signal when the threshold value is as small as 4.4 mV remains unclear. This ghost 'tail' might make it difficult to estimate the distribution of dust grains along the line of sight. The occurrence conditions of the ghost 'tail' and its peak voltage will be confirmed during the mission phase by using a return pulse from the surface of the target asteroid.

References

C.F. Bohren, D.R. Huffman, *Absorption and Scattering of Light by Small particles* (A Wiley-Interscience Publication, New York, USA, 1983), p. 530

C.R. Chapman, S-Type Asteroids, Ordinary Chondrites, and Space Weathering: The Evidence from Galileo's Fly-bys of Gaspra and Ida. Metoritics and Planetary Science **31 (6)**, 699–725 (1996)

B.E. Clark, J. Veverka, P. Helfenstein, P.C. Thomas, J.F. Bell III, A. Harch, M.S. Robinson, S.L. Murchie, L.A. McFadden, C.R. Chapman, NEAR Photometry of Asteroid 253 Mathilde. Icarus **140**, 53–65 (1999)

M. Delbo, G. Libourel, J. Wilkerson, N. Murdoch, P. Michel, K.T. Ramesh, C. Ganino, C. Verati, S. Marchi, Thermal fatigue as the origin of regolith on small asteroids. Nature **508**, 233–236 (2014)

W.K. Hartmann, Relative cratere production rates on planets. Icarus **31**, 260–276 (1977)

W.K. Hartmann, Martian cratering 8: Isochron refinement and the chronology of Mars. Icarus **174**, 294–320 (2005)

C.M. Hartzell, D.J. Scheeres, The role of cohesive forces in particle launching on the Moon and asteroids. Planetary and Space Science **59**, 1758–1768 (2011)

M. Horányi, J.R. Szalay, S. Kempf, J. Schmidt, E. Grün, R. Srama, Z. Sternovsky, A permanent, asymmetric dust cloud around the Moon. Nature **522**, 324–326 (2015)

B.A. Ivanov, Mars/Moon cratering rate ratio estimates. Chronology and Evolution of Mars **96**, 87–104 (2001)

H. Kimura, H. Senshu, K. Wada, Electrostatic lofting of dust aggregates near the termination of airless bodies and its implication for the formation of exozodiacal disks. Planetary and Space Science **100**, 64–72 (2014)

K.N. Liou, *An introduction to atmospheric radiation* (Academic Press, California, USA, 2002), p. 392

D.S. McKay, G. Heiken, A. Basu, G. Blanford, S. Simon, R. Reedy, B.M. French, J. Papike, The Lunar Regolith, in *Lunar Sourcebook*, ed. by Grant H. Heiken, G H. and Vaniman, D. T. and French, B. M. (Cambridge University Press, New York, USA, 1991), pp. 285–356

B. Michel, T.H. Henning, R. Stognienko, F. Rouleau, Extinction properties of dust grains: A new computational technique. The Astrophysical Journal **468**, 834–841 (1996)

P. Michel, D.P. O'Brien, S. Abe, H. Hirata, Itokawas cratering record as observed by Hayabusa: Implications for its age and collisional history. Icarus **200**, 503–513 (2009)

H. Miyamoto, H. Yano, D.J. Scheeres, S. Abe, O. Barnouin-Jha, A.F. Cheng, H. Demura, R.W. Gaskell, N. Hirata, M. Ishiguro, T. Michikami, A.M. Nakamura, R. Nakamura,

J. Saito, S. Sasaki, Regolith Migration and Sorting on Asteroid Itokawa. Science **316**, 1011–1014 (2007)

T. Mizuno, T. Kase, T. Shiina, M. Mita, N. Namiki, H. Senshu, R. Yamada, H. Noda, H. Kunimori, F. Terui, Y. Mimasu, Development of the Laser Altimeter (LIDAR) for Hayabusa2. Space Science Reviews **this issue** (2015)

T.G. Müller, J. Durech, S. Hasegawa, M. Abe, K. Kawakami, T. Kasuga, D. Kinoshita, D. Kuroda, S. Urakawa, S. Okumura, Y. Sarugaku, S. Miyasaka, Y. Takagi, P.R. Weissman, Y.-J. Choi, S. Larson, K. Yanagisawa, S. Nagayama, Thermo-physical properties of 162173 (1999JU3), a potential flyby and rendezvous target for interplanetary missions. Astron. Astrophys. **525**, 145 (2011)

K. Nagao, R. Okazaki, T. Nakamura, Y.N. Miura, T. Osawa, K.-i. Bajo, S. Matsuda, M. Ebihara, T.R. Ireland, F. Kitajima, H. Naraoka, T. Noguchi, A. Tsuchiyama, H. Yurimoto, M.E. Zolensky, M. Uesugi, K. Shirai, M. Abe, T. Yada, Y. Ishibashi, A. Fujimura, T. Mukai, M. Ueno, T. Okada, M. Yoshikawa, J. Kawaguchi, Irradiation History of Itokawa Regolith Material Deduced from Noble Gases in the Hayabusa Samples. Science **333**, 1128–1131 (2011)

N. Namiki, T. Mizuno, N. Hirata, H. Noda, H. Senshu, R. Yamada, H. Ikeda, S. Abe, K. Matsumoto, S. Oshigami, M. Shizugami, F. Yoshida, N. Hirata, H. Miyamoto, S. Sasaki, H. Araki, S. Tazawa, Y. Ishihara, M. Kobayashi, K. Wada, H. Demura, J. Kimura, M. Hayakawa, N. Kobayashi, Scientific Use Of LIDAR data Of Hayabusa-2 Mission, in *New Results in the Observations and Space Exploration of Asteroids*, ed. by W.-H. Ip (Macau University of Science and Technology, Macao, 2012), pp. 74–96

G. Neukum, B.A. Ivanov, W.K. Hartmann, Cratering records in the inner solar system in relation to the lunar reference system. Chronology and Evolution of Mars **96**, 55–86 (2001)

T. Okada, Overviews of Hayabusa2: The C-Class Asteroid Sample Return Mission of Japan, in *New Results in the Observations and Space Exploration of Asteroids*, ed. by W.-H. Ip (Macau University of Science and Technology, Macao, 2012), pp. 60–73

J.E. Richardson, H.J. Melosh, R. Greenberg, Impact-induced seismic activity on asteroid 433 Eros: a surface modification process. Science **306**, 1526–1529 (2004)

J.R. Szalay, M. Horányi, The search for electrostatically lofted grains above the Moon with the Lunar Dust Experiment. Geophysical Research Letters **42**, 5141–5146326 (2015)

P.C. Thomas, J. Veverka, D. Simonelli, P. Helfenstein, B. Carcich, M.J.S. Belton, M.E. Davies, C. Chapman, The Shape of Gaspra. Icarus **107 (1)**, 23–36 (1994)

Y. Tsuda, M. Yoshikawa, M. Abe, H. Minamino, S. Nakazawa, System design of the Hayabusa 2–Asteroid sample return mission to 1999 JU3. Acta Astronautica **91**, 356–362 (2013)

J. Veverka, M. Robinson, P. Thomas, S. Murchie, J.F. Bell III, N. Izenberg, C. Chapman, A. Harch, M. Bell, B. Carcich, A. Cheng, B. Clark, D. Domingue, D. Dunham, R. Farquhar, M.J. Gaffey, E. Hawkins, J. Joseph, R. Kirk, P. Li, P. Lucey, M. Malin, P. Martin, L. McFadden, W.J. Merline, J.K. Miller, W.M. Owen Jr., C. Peterson, L. Prockter, J. Warren, D. Wellnitz, B.G. Williams, Y.D. K., NEAR at Eros: Imaging and Spectral Results. Science **289**, 2088–2097 (2000)

J. Veverka, B. Farquhar, M. Robinson, P. Thomas, S. Murchie, A. Harch, P.G. Antreasian, S.R. Chesley, J.K. Miller, W.M. Owen Jr, B.G. Williams, D. Yeomans, D. Dunham, G. Heyler, M. Holdridge, R.L. Nelson, K.E. Whittenburg, J.C. Ray, B. Carcich, A. Cheng, C. Chapman, J.F. Bell III, M. Bell, B. Bussey, B. Clark, D. Domingue, M.J. Gaffey, E. Hawkins, N. Izenberg, J. Joseph, R. Kirk, P. Lucey, M. Malin, L. McFadden, W.J. Merline, C. Peterson, L. Prockter, J. Warren, W. D., The landing of the NEAR-Shoemaker spacecraft on asteroid 433 Eros. Nature **413**, 390–393 (2001)

R. Yamada, H. Senshu, N. Namiki, T. Mizuno, S. Abe, F. Yoshida, H. Noda, N. Hirata, S. Oshigam, N. Hirata, Y. Ishihara, K. Matsumoto, Performance of Hayabusa2 LIDAR to observe normal albedo on the C-type asteroid. Space Science Reviews **this issue** (2015)